CrystEngComm



PAPER

View Article Online
View Journal | View Issue



Cite this: CrystEngComm, 2025, 27, 5485

Ruthenium-modified oxygen-deficient NiCoP catalysts for efficient electrocatalytic water splitting†

Bo-yao Zhang,^a Song-lin Xu,^a Jia Li,^a Xin-Xin Zhao,^a Rong-da Zhao, ¹D*^a Ming-chang Zhang,*c De-peng Zhao ¹D*^b and Lihua Miao ¹D*^d

Ruthenium-doped nickel cobalt compounds are promising catalysts for the hydrogen evolution reaction. We report a synergistic strategy of "defect engineering + noble metal modification" to develop Rumodified oxygen-deficient NiCoP catalysts (Ru-NiCoP-O_v). By precisely controlling the synthesis conditions, we systematically investigated the impact of Ru modification and oxygen vacancies on the electrocatalytic performance of NiCoP catalysts. The prepared Ru-NiCoP-O_v catalyst exhibits excellent hydrogen evolution catalytic performance in conventional alkaline electrolyte (1 M KOH): it requires only a low overpotential of 51.5 mV at a current density of -10 mA cm⁻² for the hydrogen evolution reaction (HER). More importantly, the catalyst also performs excellently in simulated seawater electrolysis environments (1 M KOH seawater solution), with an HER overpotential of 68.1 mV at -10 mA cm⁻² current density. This outstanding performance fully demonstrates the importance of the synergistic effect of Ru modification and oxygen vacancies in enhancing catalytic activity, providing new design strategies and experimental evidence for developing efficient seawater electrolysis catalysts, and offering a feasible approach to achieving efficient and low-cost hydrogen energy production.

Received 17th May 2025, Accepted 10th July 2025

DOI: 10.1039/d5ce00510h

rsc.li/crystengcomm

1. Introduction

As the global energy crisis and environmental pollution become increasingly severe, developing clean and renewable energy conversion technologies has become a key focus in current scientific research. Electrochemical water splitting is an efficient and environmentally friendly method for hydrogen production, and it has attracted widespread attention. This process involves two half-reactions: the oxygen evolution reaction (OER) at the anode and the hydrogen evolution reaction (HER) at the cathode. The overall water electrolysis reaction depends on the kinetic coupling of these two half-reactions. Since this thermodynamically non-spontaneous process requires external electrical energy to overcome the Gibbs free energy barrier ($\Delta G > 0$), minimizing the overpotential is crucial. The closer the

operating voltage is to the theoretical decomposition voltage of

^{1.23} V, the more efficiently the reaction can be driven.³⁻⁵ Among various catalyst materials, transition metal phosphides have emerged as promising alternatives to noble metal-based catalysts. These materials offer good electrical conductivity, abundant active sites, and excellent catalytic performance. 6-9 To further enhance their activity, researchers have explored several strategies, including morphology control, elemental doping, defect engineering, and interface regulation. Creating surface defects-particularly oxygen vacancies-has proven to be an effective way to improve catalytic performance. 10,11 Oxygen vacancies not only modify the electronic structure of the material but also provide additional active sites, significantly boosting catalytic activity. In parallel, introducing small amounts of noble metals has also been widely used to enhance the performance of non-noble metal catalysts. Noble metal atoms, such as Ru, can alter the electronic structure and adsorption properties of the catalyst surface through electron transfer and interfacial synergistic effects, thereby improving reaction kinetics. 12-14 Meanwhile, transition metal phosphides are a more attractive class of catalysts compared to other transition metal compounds such as transition metal oxides and transition metal sulfides. This is due to the fact that phosphorus (P) promotes catalytic activity by modulating the d-electron orbitals.15 Recent studies have also demonstrated that modulating the local electronic states can significantly

^a School of Materials Science and Engineering, Liaoning University of Technology, Jinzhou, Liaoning 121000, China. E-mail: Rongdazhaoln@126.com

^b School of New Energy, Shenyang Institute of Engineering, Shenyang, Liaoning, 110136. P. R. China

^c Institute of Science and Technology for New Energy, Xi'an Technological University, Xi'an 710021, P. R. China. E-mail: zhangmingchang@xatu.edu.cn

^d School of Medical Information Engineering, Shenyang Medical College, Shenyang, Liaoning, 110043, P. R. China

[†] Electronic supplementary information (ESI) available. See DOI: https://doi.org/10.1039/d5ce00510h

Paper

enhance electrocatalytic activity. For example, rare-earth (RE) elements can induce asymmetric structures, such as RE-O-Ru

units, which facilitate the accumulation of localized electronic states around bridging oxygen vacancies (O_v) through electron delocalization effects. This promotes the deprotonation of *OH intermediates and lowers the reaction energy barrier. Similarly, metal doping can be employed to tailor the electron density, thereby optimizing the electronic structure and improving electrocatalytic performance by mitigating the strong adsorption of intermediates. 16-18 In recent years, the synergistic strategy of combining defect engineering with noble metal modification has gradually attracted the attention of researchers. This "double optimization" strategy can simultaneously leverage the advantages of defects and noble metals to achieve a multiplier effect on catalytic performance. 19 In this strategy, oxygen vacancies can serve as anchoring sites for noble metal atoms, not only improving the dispersion and utilization rate of noble metals but also further regulating the electronic structure of the catalyst through strong interactions between defects and metals. 10 Moreover, the unsaturated coordination environment around oxygen vacancies is conducive to the adsorption and activation of water molecules, thereby accelerating the progress of electrochemical reactions.20 Wang et al.21 synthesized CoP-NiCoP heterojunctions with a pine needle-like morphology through a hydrothermal phosphorization method, achieving a HER potential of 0.13 V at a current density of 50 mA cm⁻². Wang et al. 22 synthesized a Ga-intercalated NiCoP catalyst using a hydrothermal method followed by phosphidation. The resulting Ga-intercalated NiCoP-15% electrode exhibited an overpotential of only 71 mV at a current density of -10 mA cm⁻². Lin et al.²³ proposed a strategy for modifying heterojunction interfaces using oxygen atoms. The constructed O-Co/NiCoP nanosheets exhibited excellent electrocatalytic activity, providing high current densities of 300 mA cm⁻² for both HER and OER at 361 and 430 mV in 1 M KOH, respectively.

Here, we adopt a synergistic strategy of "defect engineering + noble metal modification", using nickel foam as the substrate, and successfully prepare a series of Ru-modified oxygendeficient NiCoP catalysts (Ru-NiCoP-O_v) through hydrothermal methods and low-temperature phosphorization. By precisely controlling the synthesis conditions, we systematically investigate the impact of Ru modification and oxygen vacancies on the electrocatalytic performance of NiCoP catalysts. Electrochemical tests show that the prepared Ru-NiCoP-O_v catalyst exhibits excellent bifunctional catalytic performance in conventional alkaline electrolyte (1 M KOH): in the hydrogen evolution reaction (HER), the catalyst requires only a low overpotential of 51.5 mV at a current density of 10 mA cm⁻²; in the oxygen evolution reaction (OER), the overpotential is merely 231.1 mV at the same current density. More importantly, the catalyst also performs excellently in simulated seawater electrolysis environments (1 M KOH seawater solution), with HER overpotentials of 68.1 mV at 10 mA cm⁻² current density and OER overpotentials of 276.1 mV at 50 mA cm⁻² current density.

2. Experimental section

2.1. Synthesis of NiCo precursor

In this study, Ru-modified oxygen-deficient NiCoP catalysts were prepared using a combination of hydrothermal method and low-temperature phosphorization, achieving in situ growth on nickel foam. All reagents used were of analytical grade and could be used directly without further purification. The specific preparation steps are as follows:

Firstly, the nickel foam substrate was pre-treated. The standardized 3 cm × 3 cm square nickel foam samples were ultrasonically cleaned in a 3.0 M hydrochloric acid solution and deionized water for 15-20 minutes to activate the surface and remove the oxide layer. Subsequently, 1 mmol of Ni(NO₃)₂·6H₂O, 2 mmol of Co(NO₃)₂·6H₂O, 8 mmol of NH₄F, and 16 mmol of urea were accurately weighed and dissolved in 60 mL of deionized water, forming a uniform precursor solution under magnetic stirring for 1 hour at room temperature. The pre-treated nickel foam was then vertically immersed into the reaction solution and placed inside a high-pressure reactor where it underwent hydrothermal reaction at 130 °C for 5 hours. After the reaction, it was allowed to naturally cool down to room temperature, washed three times each with anhydrous ethanol and deionized water, and dried overnight in a 60 °C oven to obtain the NiCo precursor material.

2.2. Preparation of Ru-NiCoP-O_v

To prepare the Ru-modified oxygen-deficient NiCoP catalyst (Ru-NiCoP-O_v), 0.3 mmol of RuCl₃·3H₂O was dispersed in a water-ethanol mixed solution with a volume ratio of 1:1 (totaling 60 mL). Under vigorous stirring, 0.1 mmol of NaBH₄ was quickly added as a reducing agent. The nickel foam loaded with the NiCo precursor was then immersed in this solution and reacted for 5 hours at room temperature. Subsequently, the sample was placed in a 60 °C oven to dry. Finally, the dried sample was placed in a tube furnace, using 0.5 g of NaH₂PO₂ as the phosphorus source. Under a high-purity argon atmosphere following three vacuum-argon purge cycles, the temperature was raised at a rate of 2 °C min⁻¹ to 350 °C and maintained at this temperature for phosphorization for 120 minutes. The resulting product was labeled as Ru-NiCoP-Ov-

2.3. Preparation of NiCoP-O_v/Ru-NiCoP/NiCoP

To systematically investigate the impact of Ru modification and oxygen defects on catalytic performance, a series of control samples were also prepared in this study. For the preparation of the NiCoP-O_v sample, the NiCo precursor was first synthesized using a hydrothermal method. The precursor was then immersed in a water-ethanol (1:1, v/v) mixed solution containing only 0.1 mmol of NaBH4 but without RuCl3·3H2O, and reacted for 5 hours at room temperature. After drying at 60 °C, the sample was processed under the same phosphorization conditions as described previously, and the final product was labeled as NiCoP-O_v.

For the preparation of the Ru-NiCoP sample, the hydrothermally synthesized NiCo precursor was immersed in a water-ethanol (1:1, v/v) mixed solution containing only 0.3 mmol of RuCl₃·3H₂O without NaBH₄, and reacted for 5 hours at room temperature. After drying at 60 °C, the sample was processed under the same phosphorization conditions as previously described, and the final product was labeled as Ru-NiCoP.

For the preparation of the NiCoP sample, the hydrothermally synthesized NiCo precursor was immersed in a water-ethanol (1:1, v/v) mixed solution without RuCl₃·3H₂O and NaBH₄, and reacted for 5 hours at room temperature. After drying at 60 °C, the sample was phosphorized under a high-purity argon atmosphere using NaH2PO2 as the phosphorus source. The phosphorization was carried out at 350 °C for 120 minutes. The resulting product was labeled as NiCoP.

Additionally, during the experimental process, a sample was retained that only underwent the hydrothermal synthesis method to prepare the NiCo precursor, without any further processing. This sample was directly labeled as NiCo-Precursor and used as a control sample. All prepared samples were stored in a vacuum drying oven for subsequent characterization and electrochemical testing. Scheme 1 illustrates the process flow diagram for the Ru-NiCoP-O_v material.

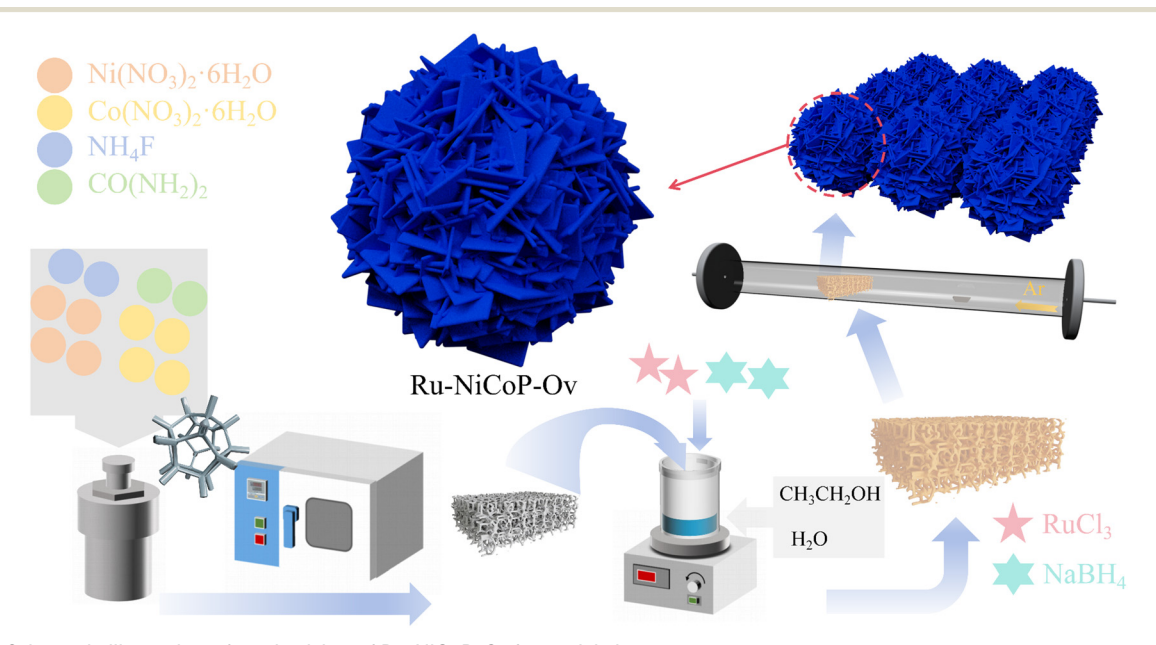
2.4. Material characterization and electrocatalytic performance characterization

The crystal structure of the prepared samples was characterized by X-ray diffraction (XRD, Shimadzu-7000, Cu Kα) in the range of 10° to 90° with a scanning speed of 8° min⁻¹. The surface chemical states, elemental valence states, and qualitative and quantitative information of elements were determined by X-ray photoelectron spectroscopy (XPS, ESCALAB 250 with an Al Kα). Scanning electron microscopy (SEM, Gemini 300-71-31) was used to characterize the micromorphological changes of the prepared samples.

All electrochemical tests were performed on a Chenhua electrochemical workstation (CHI760E). The tests were conducted in a three-electrode system using 1 M KOH (pH = 13.7) and 1 M KOH (pH = 13.51) seawater alkaline solutions as electrolytes (the main composition of the alkaline seawater solution is listed in Table 1). A Hg/HgO electrode was used as the reference electrode, a graphite rod and Pt electrode served as the counter electrodes. The prepared samples (0.5 cm × 0.5 cm) were used as working electrodes for electrochemical testing. The linear sweep voltammetry (LSV) curves were obtained using an electrochemical workstation with IR compensation set at 90%. Partially corrected polarization curves are not suitable for Tafel analysis, as residual IR effects can distort the current-potential relationship. 24,25 Therefore, all Tafel analyses in this study are based on fully (100%) IR-corrected data and converted to the reversible hydrogen electrode (RHE) scale using the Nernst equation: $E_{\text{RHE}} = E_{\text{Hg/HgO}} + 0.059 \times \text{pH} + 0.098$. The OER overpotential was calculated using $\eta = E_{RHE} - 1.23 \text{ V}$.

3. Results and discussion

The phase composition of the prepared samples was first characterized by XRD patterns. As shown in Fig. 1, the peaks observed at 2θ values of 44.4°, 51.6°, and 76.1° correspond to the strong diffraction peaks of the Ni foam substrate (JCPDS no. 04-0850). The XRD diffraction peaks of the NiCoP, Ru-NiCoP, NiCoP-O_v, and Ru-NiCoP-O_v samples are highly consistent with the standard hexagonal NiCoP phase (JCPDS



Scheme 1 Schematic illustration of synthesizing of Ru-NiCoP-O_v foam nickel.

Table 1 ICP-OES analysis of alkaline seawater solution

Elements	Dilution ratio	Elemental concentration (mg L^{-1})
Ca	1	5.195
K	1000	12.76
Mg	1	5.885
Na	1000	4.343
Ca	1	5.191
K	1000	12.72
Mg	1	5.888
Na	1000	4.348

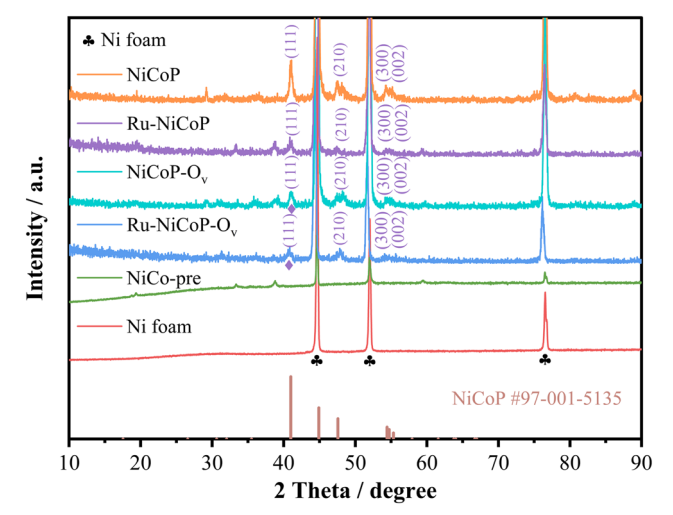


Fig. 1 XRD patterns of each sample.

#97-001-5135), indicating that the phosphidation treatment was successfully achieved and the desired crystallographic structure was obtained. Specifically, all samples exhibit characteristic peaks near $2\theta = 40.8^{\circ}$, 47.5° , 54.2° , and 54.8° , which correspond to the (111), (210), (300), and (002) crystal planes of NiCoP, respectively. The positions and relative intensities of these peaks match well with those of the standard reference, further confirming that the main crystalline phase in the samples is indeed NiCoP. Meanwhile, NiCo-Precursor mainly consists of nickel-cobalt hydroxides, which provides a structural basis for the subsequent phase transformation from hydroxides to phosphides during phosphidation. Notably, compared to the NiCoP-O_v sample, the main diffraction peak corresponding to the (111) plane of Ru-NiCoP-Ov shows a slight shift toward lower angles, which is consistent with the lattice expansion effect induced by Ru doping. Given that the atomic radius of Ru (134 pm) is slightly larger than those of Ni (124 pm) and Co (125 pm) atoms, when it partially substitutes or enters the NiCoP lattice, the lattice parameters increase, resulting in an increased interplanar spacing (d-value). According to Bragg's law $(n\lambda = 2d\sin\theta)$, this leads to a minor decrease in the peak position. Moreover, no significant characteristic peaks attributable to metallic Ru or Ru

compounds were observed in any of the four samples, suggesting that Ru may exist in a highly dispersed atomic or small cluster form on the catalyst surface, below the detection limit of XRD. By comparing the XRD patterns of NiCoP with NiCoP-O_v, as well as Ru-NiCoP with Ru-NiCoP-O_v, it can be seen that the introduction of oxygen vacancies has no obvious effect on the crystal phase structure, indicating that the introduction of oxygen vacancies mainly affects surface properties rather than altering the overall crystal structure. Additionally, based on the estimation from Scherrer's formula, the peak widths of the four samples are close, suggesting they have similar crystallite sizes, indicating that Ru doping and the introduction of oxygen vacancies did not significantly alter the degree of crystallinity and grain growth process of the NiCoP material.

Then, X-ray photoelectron spectroscopy (XPS) was employed to systematically investigate the surface electronic structure and chemical states of elements in the Ru-NiCoP-O_v material. This analysis aimed to reveal the intrinsic mechanisms through which Ru doping and oxygen vacancies modulate the electronic properties of the NiCoP substrate and enhance its electrocatalytic performance. As shown in the full XPS spectrum (Fig. 2a), distinct signals corresponding to Ni 2p, Co 2p, P 2p, O 1s, C 1s, and Ru 3d were observed, confirming the successful incorporation of all target elements on the material's surface. Further detailed analysis of individual element spectra provides insight into their bonding configurations and interfacial interactions. In the Ni 2p spectrum of Fig. 2b, a signal at 852.90 eV corresponds to a typical Ni—P bond, with its binding energy range consistent with metallic Ni and Ni 2P-like metal coordination states, confirming that the phosphorization process enabled partial covalent bonding of Ni.26 Peaks at 856.00 eV and 861.40 eV are attributed to the main peak and satellite peak of Ni²⁺, respectively, indicating that surface Ni oxidation is inevitable.8 However, such oxides often work synergistically with oxygen vacancies to provide tunable active centers for intermediate adsorption and electron transfer during reactions. The peaks at 869.99 eV (Ni-P) and 873.80 eV (Ni²⁺) in the Ni 2p_{1/2} region, as well as higher binding energy satellite peaks, are consistent with the above analysis, further confirming that Ni exists in a state of coexistence between metal phosphide and partial oxidation. As shown in Fig. 2c, the peak at 778.90 eV in the Co 2p spectrum corresponds to Co-P bonds, confirming that Co is stably embedded in the NiCoP phase in the form of phosphides; peaks at 782.40 eV and corresponding satellite peaks indicate varying degrees of surface Co oxidation (such as CoO or Co(OH)2), echoing the oxidation characteristics of Ni.27,28 Subsequent analysis in the Co 2p_{1/2} region shows that peaks at 797.10 eV and 802.45 eV correspond to Co-P and oxidized Co species, respectively, while the high binding energy peak at 806.25 eV may originate from multiple splitting or secondary satellite peaks. Thus, while the main body of NiCoP retains the phosphide lattice, its surface oxidation states and defect structures are formed during synthesis and treatment, which is an

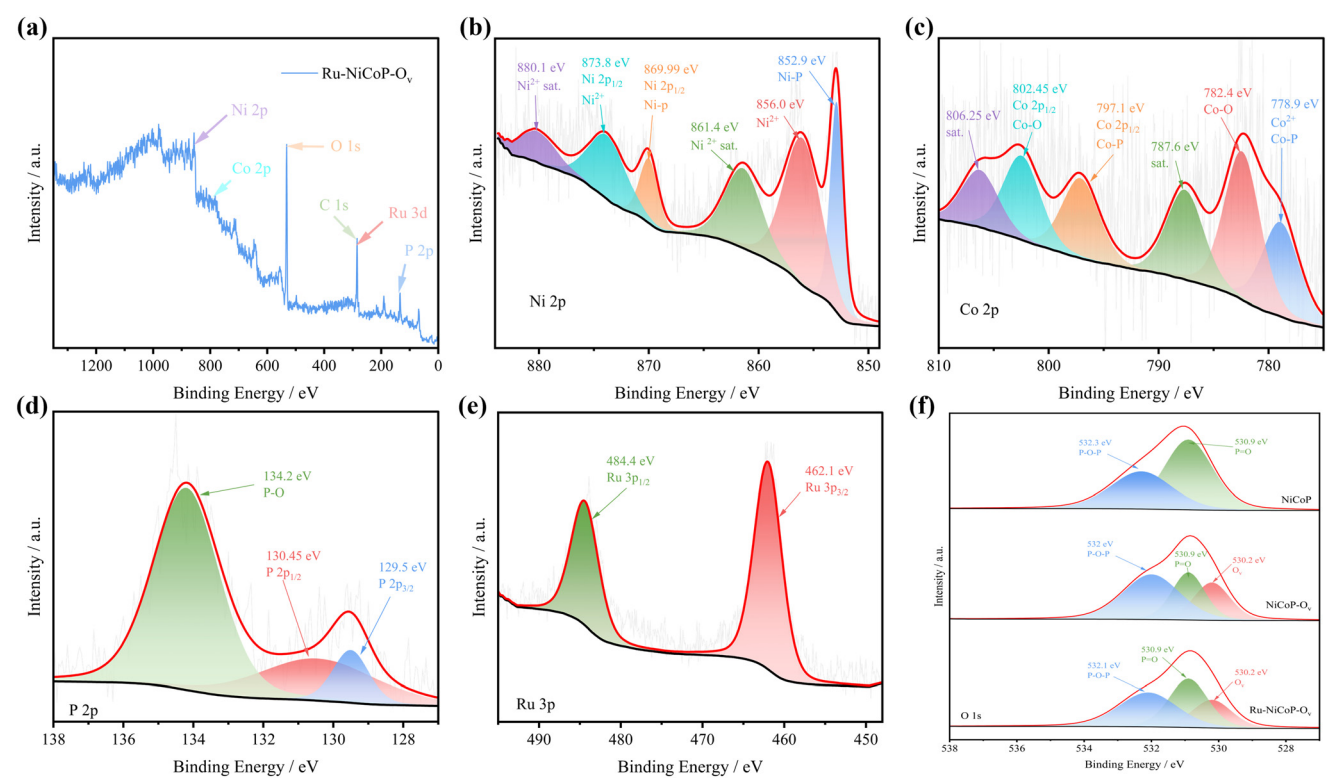


Fig. 2 (a) The high resolution XPS survey spectra. (b) XPS of Ni 2p (c) Co 2p (d) P 2p (e) Ru 3d. (f) Comparison of O 1s XPS spectra among NiCoP, NiCoP-O_v, and Ru-NiCoP-O_v samples.

important factor in enhancing catalytic surface activity. In the P 2p spectrum of Fig. 2d, peaks at 129.50 eV and 130.45 eV correspond to P 2p_{3/2} and P 2p_{1/2} main peaks, respectively, with these binding energies consistent with typical P-M (M = Ni or Co) bonds in NiCoP-like metallic phosphides, indicating that Ni and Co form stable phosphide structures with phosphorus during phosphorization.²⁹ A peak appearing at approximately 134.20 eV in the high binding energy region points to surface oxidized phosphorus species (P-O or POx), indicating partial oxidation of the surface layer during synthesis and air exposure but without destroying the main NiCoP framework. Ru 3p XPS spectra reveal that Ru in the prepared catalyst predominantly exists in the metallic state Ru^0 . The Ru $3p_{3/2}$ and Ru $3p_{1/2}$ peaks are located at 462.1 eV and 484.4 eV, respectively, which are in excellent agreement with the binding energy values reported in the literature for metallic Ru.30 The spin-orbit splitting energy of 22.3 eV and an approximate peak area ratio of 2:1 further confirm the characteristic features of Ru 3p orbitals. This dominant metallic Ru⁰ species is crucial for enhancing the catalytic activity of the material. In the O 1s spectrum, the binding energy at 532.3 \pm 0.2 eV corresponds to the P-O-P bridging oxygen, 530.9 ± 0.1 eV is attributed to P=O species, and 530.2 ± 0.1 eV represents low-coordinated lattice oxygen or oxygen vacancies.³¹ Comparative analysis reveals that the asprepared NiCoP sample exhibits only the P-O-P and P=O peaks, indicating that the surface is dominated by intact phosphorus-oxygen tetrahedral structures without detectable oxygen vacancies. The introduction of oxygen vacancies significantly altered the O 1s XPS spectrum of the NiCoP sample. Compared to the pristine NiCoP, a new characteristic peak at 530.2 eV emerged in the defect-engineered NiCoP-O_v sample, which is attributed to the chemical state associated oxygen vacancies, indicating their successful incorporation into the material. In the Ru-modified Ru-NiCoP-O_v sample, the intensity of this peak was reduced but still clearly present, suggesting that the introduction of Ru may enhance the catalytic performance by stabilizing the existing oxygen vacancies. In addition, as shown in Fig. S2,† Electron Paramagnetic Resonance (EPR) spectroscopy was employed to characterize both the Ru-NiCoP and Ru-NiCoP-Ov catalysts. While Ru-NiCoP exhibited a weak signal indicative of oxygen vacancies, Ru-NiCoP-O_v displayed a prominent EPR signal at g = 2.005. This distinct signal is attributed to electrons trapped within oxygen vacancies, confirming their significant presence in the Ru-NiCoP-Ov material.

Scanning Electron Microscopy (SEM) and Transmission Electron Microscopy (TEM) were employed to characterize the micro-morphological changes of a series of materials. Through SEM, it can be observed that the unmodified NiCoP sample (Fig. 3a) exhibits a relatively disordered network of nanoneedles, which, although maintaining a one-dimensional growth trend, lacks distinct central radiation features, with randomly distributed and densely packed nanoneedles. Fig. 3b shows the morphological characteristics of the Ru-NiCoP

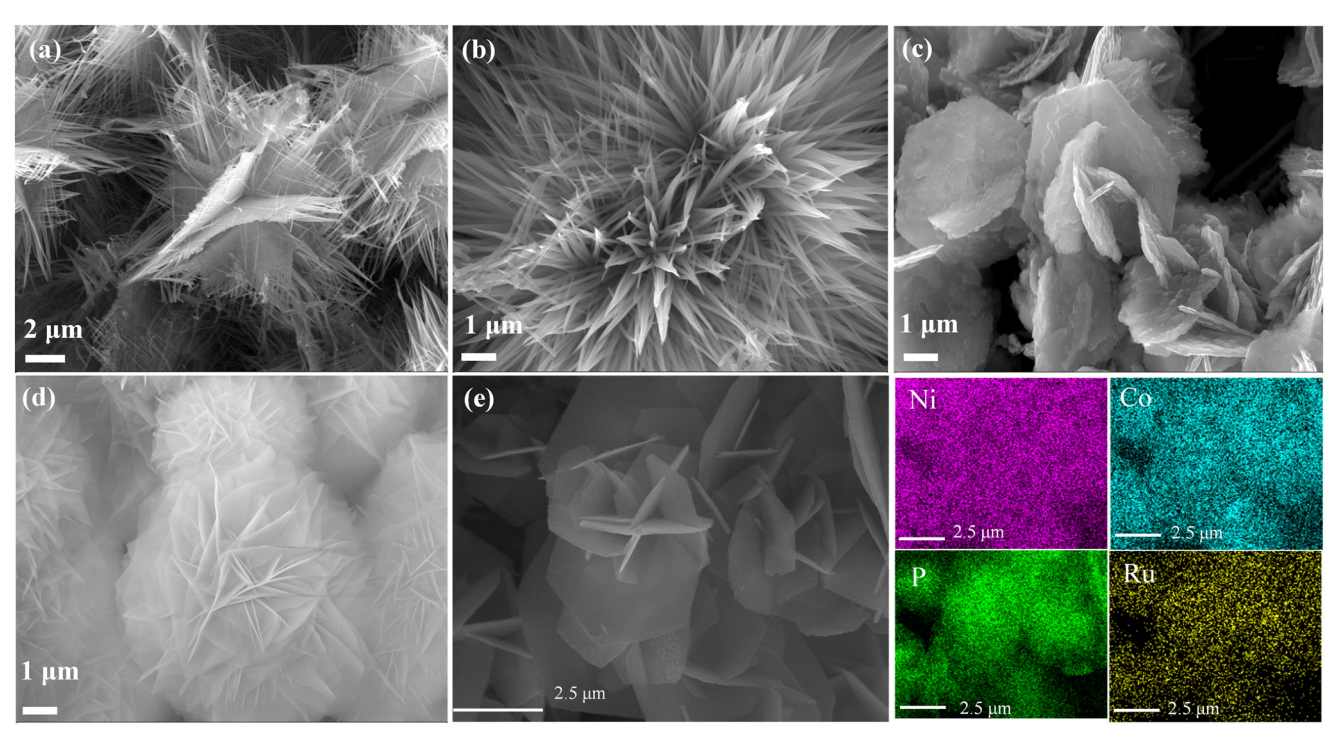


Fig. 3 Morphology and structure characterization of the as-prepared products (a) SEM images of NiCoP (b) Ru-NiCoP (c) NiCoP-O, (d) Ru-NiCoP-O_v (e) EDS elemental mapping of Ru-NiCoP-O_v.

presenting a clear radiating needle-like crystal structure. These one-dimensional nanoneedles grow radially from the center to the periphery, forming a "sea urchin"-like three-dimensional structure. The NiCoP-O_v sample (Fig. 3c) displays a relatively flat stacked nanosheet structure. Although it maintains a lamellar morphology, the gaps between the layers are significantly reduced compared to the Ru-NiCoP-Ov sample (Fig. 3d). The Ru-NiCoP-O_v sample presents a unique multi-level nanosheet structure, where these nanosheets interweave to form a threedimensional network structure. The thickness of the lamellae is about 10-20 nm, with edges showing obvious wrinkles and curling features. This highly wrinkled nanosheet structure provides abundant exposed edge sites and a large surface area, which is very conducive to electrolyte penetration and the progress of electrochemical reactions. Fig. 3e presents the SEM image and EDS elemental mapping of the Ru-NiCoP-O_v catalyst. The left-hand SEM image clearly reveals its unique threedimensional wrinkled nanosheet structure. The corresponding EDS elemental mapping images on the right show the spatial distribution of each element. Phosphorus (P Kα₁, green), cobalt (Co $K\alpha_1$, blue), nickel (Ni $K\alpha_1$, purple), and ruthenium (Ru $L\alpha_1$, yellow) are uniformly distributed across the surface without noticeable aggregation, indicating a homogeneous composition throughout the catalyst. Notably, the even distribution of ruthenium confirms the successful and uniform incorporation of Ru atoms onto the NiCoP nanosheet surface, which is essential for achieving uniformly dispersed catalytic active sites. At the same time, as shown in Table S1,† the Ru mass loading was calculated to be 0.02 mg mm⁻² based on the mass difference per unit area, and the parameters of HAADF-STEM in

Fig. S1[†] showed that the Ru precursor loading was 2.7%. This provides a reference for the uniform distribution and loading amount of catalytic active sites. To further investigate the microstructural features of the Ru-NiCoP-O_v catalyst and assess its structural stability before and after electrochemical cycling, detailed TEM analysis was conducted. Fig. 4a shows the lowmagnification TEM image of the Ru-NiCoP-Ov sample before cycling, revealing uniformly dispersed nanostructures. Fig. 4b presents the high-resolution TEM image before cycling, clearly displaying the lattice fringes of the sample, with the measured (111) plane spacing being 0.2235 nm, consistent with the calculated value of the NiCoP phase (111) plane spacing from XRD analysis, indicating good crystallinity of the sample. Fig. 4c depicts the integrated HAADF-STEM elemental distribution map of the sample before cycling, showing the distribution of each element within the nanoparticles. Fig. 4d-g respectively show the individual distribution maps of Ni, Co, P, and Ru elements in the sample before cycling. Among them, Ni and Co elements are more densely and uniformly distributed, P element is uniformly spread across the entire sample, while the distribution of Ru element is relatively sparse, consistent with the designed composition of the catalyst. Fig. 4h shows the lowmagnification TEM image of the sample after electrochemical cycling, demonstrating that the sample still retains its original nanostructure morphology. Fig. 4i presents the high-resolution TEM image after cycling, showing a slight decrease in the (111) plane spacing to 0.224 nm, possibly due to partial filling of oxygen vacancies in the lattice during electrochemical cycling leading to lattice contraction. However, overall, this indicates that the electrochemical cycling process has a minor impact on

CrystEngComm

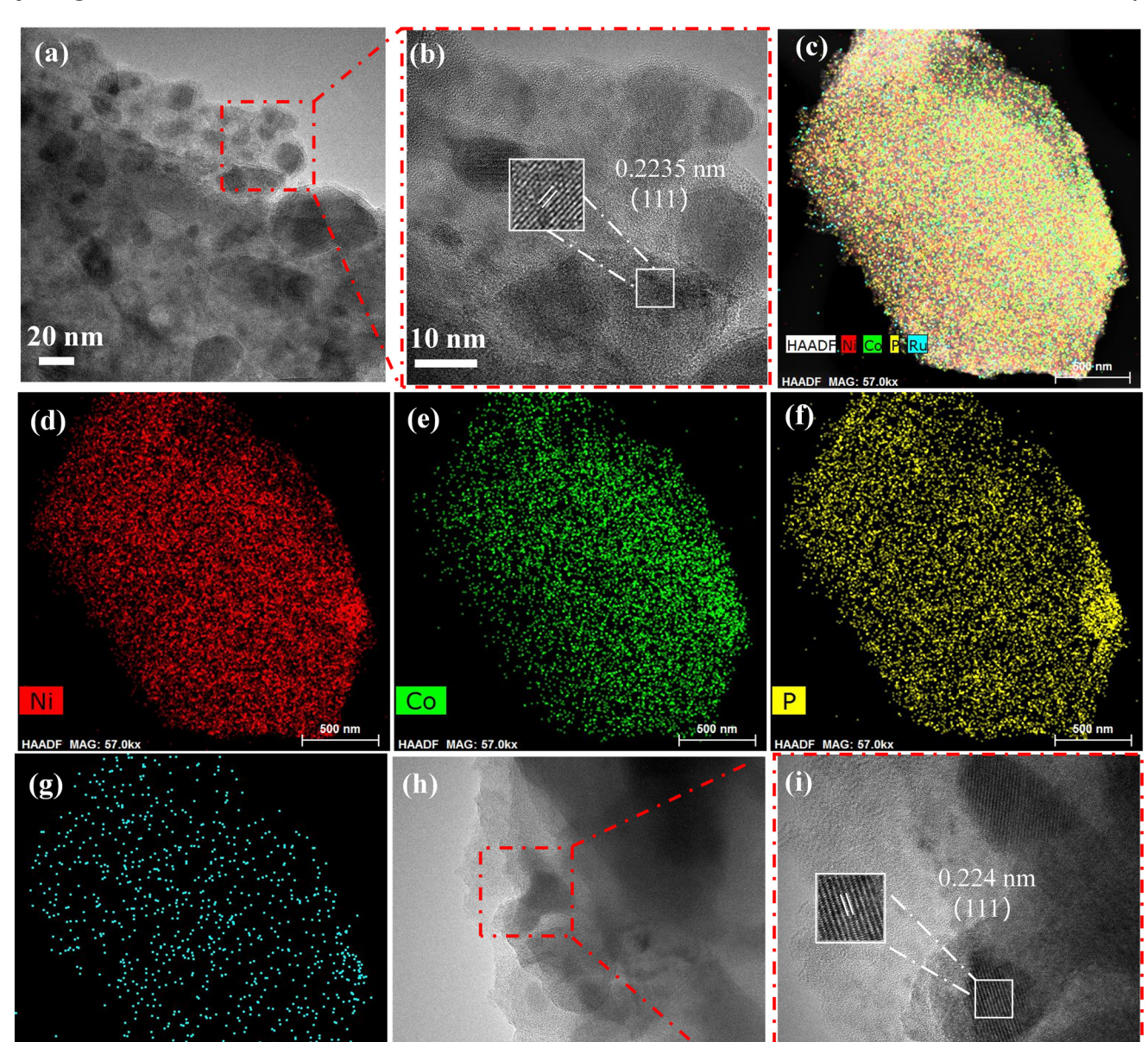


Fig. 4 (a-g) Typical transmission electron microscopy (TEM) image and the corresponding (EDX) elemental mapping of Ru-NiCoP-O_v. (h and i) Low- and high-resolution TEM images after cycling.

20 nm

the crystal structure of the sample, confirming that the catalyst possesses good structural stability during electrochemical reactions. Meanwhile, by comparing the high-magnification TEM images in Fig. 4b and i, it is evident that Fig. 4i displays a distinct sub-surface oxidation layer around its periphery. This observation indicates that the sample has undergone overoxidation, with its exterior transforming into a slightly lattice-increased Ru-NiCoP-O $_{\rm V}$ passivated interfacial layer. This layer effectively prevents further oxidation and corrosion of the internal material, acting as a protective shell. Furthermore, from the overall morphology shown in the TEM images, there are no noticeable precipitates or pore structures within the sample. 32

The synergistic effect of surface oxidation and passivation explains the mechanism behind the material's excellent performance during cycling processes. We further conducted XPS structural characterization on the sample after electrochemical cycling. As shown in the Ni 2p spectrum (Fig. 5a), compared to the as-prepared sample, the main peak at approximately 855.5 eV—attributed to Ni²⁺—exhibits significantly enhanced signal intensity after cycling. In the Ni $2p_{1/2}$ region, the Ni²⁺ peak at 873.1 eV also shows increased intensity. These observations indicate that during prolonged electrochemical cycling, some surface Ni atoms undergo further oxidation, forming more NiOOH species, which are recognized

<u>10 nm</u>



Paper

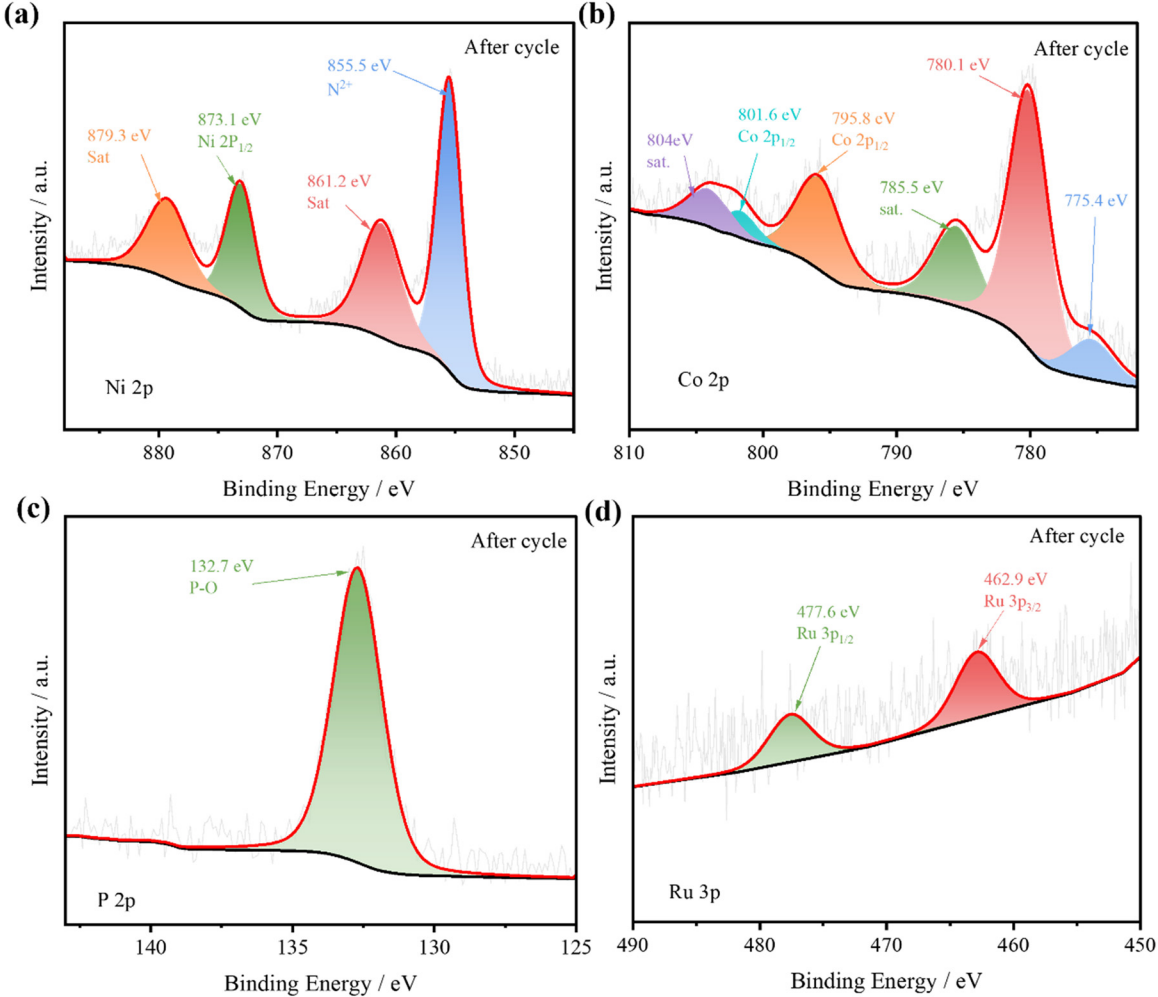


Fig. 5 XPS characterization of Ru NiCoP O_v sample after cycling (a) XPS of Ni 2p (b) Co 2p (c) P 2p (d) Ru 3d after cycling

as active catalytic sites. In the Co 2p spectrum (Fig. 5b), a strong main peak appears at around 780.1 eV in the Co 2p_{3/2} region, accompanied by a distinct satellite peak at 785.5 eV, which is characteristic of oxidized Co species, specifically a mixedvalence Co(II)/Co(III) oxide state. A weaker peak at 775.4 eV can still be observed, likely corresponding to residual Co-P bonding or an intermediate oxidation state. In the Co $2p_{1/2}$ region, the main peak at 801.6 eV further confirms the presence of oxidized Co species, while a lower binding energy peak at 795.8 eV may be attributed to phosphide or slightly oxidized Co species. These results strongly suggest that significant surface oxidation and reconstruction occur during the electrochemical cycling process, where Co phosphides are transformed into Co(II)/Co(III) mixed-oxide species that serve as key active sites on the material surface after cycling. The P 2p spectrum of the cycled sample (Fig. 5c) reveals a substantial weakening or near disappearance of the P-M (metal) bond signals typically associated with phosphides, with P-O bonds dominating in the high-bindingenergy region (132.7 eV). This indicates that the NiCoP structure on the material surface undergoes pronounced oxidative reconstruction during cycling, leading to the formation of a large amount of phosphate species. Furthermore, the Ru 3p spectrum shows noticeable shifts in both the Ru $3p_{3/2}$ and Ru $3p_{1/2}$ peaks, suggesting partial oxidation of originally metallic Ru⁰ into various oxidized Ru species. This dynamic valence-state variation and the formation of Ru oxides indicate that Ru actively participates in the catalytic process and exerts its catalytic function in oxidized forms.

To comprehensively evaluate the hydrogen evolution reaction (HER) and oxygen evolution reaction (OER) performance of the prepared catalysts, systematic tests were conducted in a threeelectrode system. Fig. 6a shows the LSV curves of the various catalysts. It can be observed that the Ru-NiCoP-Ov catalyst exhibits the most excellent HER activity, generating the highest current density at the same potential. Its curve is clearly positioned to the right of the other samples, indicating the lowest reaction initiation energy barrier, manifested as an overpotential of 51.5 mV at -10 mA cm⁻². Fig. 6b presents a comparison of the Tafel slopes of the catalysts. Further analysis reveals that the Tafel slope of the Ru-NiCoP-O_v sample is 73.8 mV dec⁻¹, significantly lower than those of NiCoP-O_v (86.89 mV dec⁻¹), Ru-NiCoP (82.93 mV dec⁻¹), NiCoP (84.04 mV dec⁻¹), and NiCo-Precursor (132.98 mV dec⁻¹). This extremely low Tafel slope suggests that the HER on the Ru-NiCoP-O_v catalyst likely

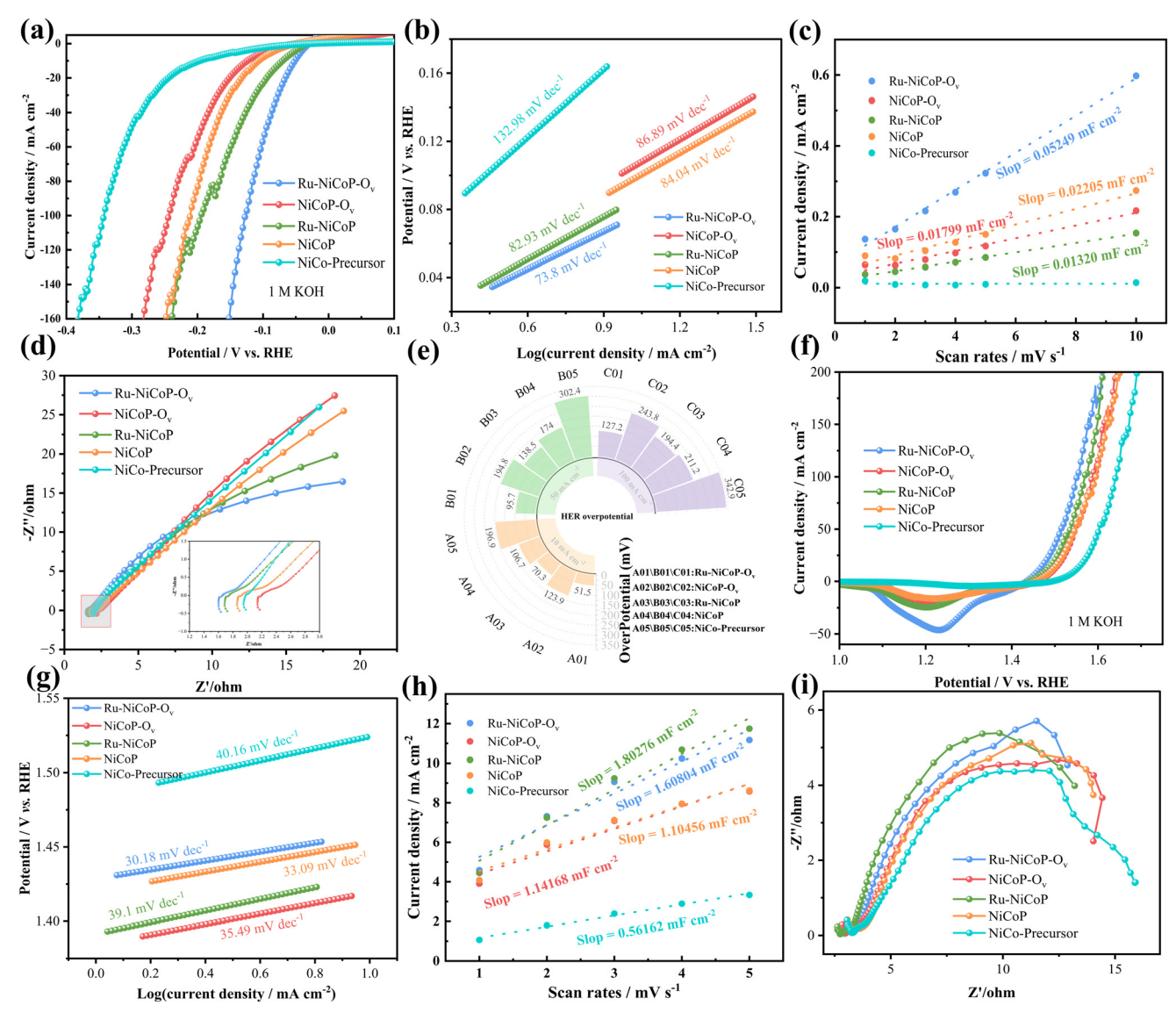


Fig. 6 HER and OER (a-i) performances in 1 M KOH solutions (a) LSV curves at scan rate of 5 mV s⁻¹ (b) Tafel plots (c) double-layer capacitance (C_{dl}) (d) Nyquist plots (e) radial diagram of overpotential of the sample (f) LSV curves of OER (g) Tafel plots. (h) Double-layer capacitance (i) Nyquist plots.

the Volmer–Tafel mechanism.³³ Moreover, desorption process of hydrogen atoms is no longer the ratedetermining step, and the reaction kinetics are significantly optimized. As shown in the SEM analysis, the highly wrinkled nanosheet structure provides abundant exposed edges and a large specific surface area, which offers favorable conditions for electron transfer and reactant diffusion, further reducing reaction resistance. Fig. 6c displays the double-layer capacitance $(C_{
m dl})$ results measured by cyclic voltammetry at different scan rates (1-10 mV s⁻¹), used to evaluate the electrochemical active surface area (ECSA) of the catalysts. The results indicate that the $C_{\rm dl}$ value of the Ru-NiCoP-O_v sample reaches 0.05249 mF cm⁻², much higher than those of other samples such as NiCoP-Ov (0.01799 mF cm⁻²), Ru-NiCoP (0.01320 mF cm⁻²), and NiCoP (0.02205 mF cm⁻²). This means that Ru-NiCoP-O_v has the largest electrochemical active surface area, providing more active sites for participation in the HER. In Fig. 6d, the Nyquist plot shows that the Ru-NiCoP-O_v sample has a small semicircle diameter in the high-frequency region of the curve, which is closely related to the charge transfer rate at the electrode surface. The smaller the diameter, the lower the charge transfer resistance, and the faster the kinetics of the electrochemical reaction. In the lowfrequency region, the following formula can be used as a reference.34

$$Z = R_{\rm s} + R_{\rm ct} + \sigma_{\rm w} \omega^{-1/2} \tag{1}$$

Here $\sigma_{\rm w}$ represents the Warburg factor, and ω denotes the angular frequency. Z is attributed to the diffusion resistance of OH⁻. Simultaneously, we employed Nyquist fitting curves to analyze the charge transfer resistance (R_{ct}) , a critical indicator for evaluating electrode kinetic rates. A lower R_{ct} value typically signifies a faster interfacial charge transfer process. As shown in Fig. S3a,† Ru-NiCoP-O_v exhibits the smallest $R_{\rm ct}$ (29.19 Ω) compared to NiCoP-O_v (46.21 Ω), Ru-NiCoP (33.24 Ω), NiCoP (34.76 Ω), and NiCo-Precursor (42.54 Ω). This confirms that Ru doping can effectively reduce the resistance of the NiCoP matrix, enhance charge transfer efficiency, and consequently improve catalytic efficiency. The inset shows the corresponding equivalent circuit diagram of the samples. Fig. 6e shows the overpotential plots of each catalyst at different current densities. The figure indicates that the Ru-NiCoP-O_v exhibits overpotentials of only 51.5, 95.7, and 127.2 mV at current densities of 10, 50, and 100 mA cm⁻², respectively, which are much lower than those of other control samples. This result confirms the significant enhancement effect of Ru modification and oxygen defects on HER performance. The presence of oxygen defects creates additional active sites and modulates the local electron density distribution, further facilitating the progress of electrocatalytic reactions. Fig. 6f presents the linear sweep voltammetry (LSV) curves of the series of catalysts. At a current density of 50 mA cm⁻², the overpotential for the Ru-NiCoP-O_v sample is 285.1 mV, which is lower than that of NiCoP-O_v (317.3 mV), Ru-NiCoP (305.3 mV), NiCoP (316.3 mV), and NiCo precursor (372.3 mV). This indicates that the Ru-NiCoP-O_v catalyst exhibits the best OER activity among the tested materials, capable of generating higher current densities at the same potential and possessing the lowest reaction onset barrier. The reduction peaks observed in the voltammogram are attributed to the electrochemical reduction of Ni³⁺ and Co³⁺ species in NiCoP to their lower valence states. The enhanced catalytic activity of the Ru-NiCoP-O_v catalyst is largely dependent on the synergistic effect between Ni and Co.35 Fig. 6g shows the Tafel slope analysis of each catalyst. The Tafel slope of the Ru-NiCoP-O_v sample is 30.18 mV dec⁻¹, significantly lower than those of NiCoP-O_v (35.49 mV dec⁻¹), Ru-NiCoP (39.1 mV dec⁻¹), NiCoP (33.09 mV dec⁻¹), and NiCo precursor (40.16 mV dec⁻¹). This extremely low Tafel slope indicates a faster electron transfer rate and more efficient reaction kinetics process for the OER on the Ru-NiCoP-O_v catalyst. Fig. 6h displays the results of voltammetry at various scan rates (1-5 mV s⁻¹). The $C_{\rm dl}$ value of the Ru-NiCoP-O_v sample reaches 1.60804 mF cm⁻², second only to Ru-NiCoP (1.80276 mF cm⁻²), but significantly higher than those of NiCoP-O_v (1.14168 mF cm⁻²), NiCoP (1.10456 mF cm⁻²), and NiCo precursor (0.56162 mF cm⁻²), suggesting that Ru-NiCoP-O_v possesses a larger electrochemical active surface area capable of providing abundant active sites for the OER reaction. Notably, the comparative analysis between Fig. 6f and h indicates that although the Ru-NiCoP sample has the highest $C_{\rm dl}$ value, its OER performance is inferior to that of Ru-NiCoP-Ov, further confirming the critical role of oxygen defects in tuning the electronic structure and optimizing catalytic activity. In the impedance diagram shown in Fig. 6i, the Ru-NiCoP-O_v sample has a notably smaller semicircle diameter range in the high-frequency region compared to other samples, indicating good reaction kinetics. Fig. S3b† shows the impedance fitting, and Ru-NiCoP-O_v exhibits a relatively low $R_{\rm ct}$ (7.973 Ω) compared to NiCoP-O_v (7.727 Ω), Ru-NiCoP (9.093 Ω), NiCoP (8.44 Ω), and NiCo-Precursor (7.608 Ω). This indicates that oxygen vacancies can appropriately reduce the charge transfer impedance of the NiCoP matrix. Although NiCo-Precursor has the lowest Rct value, in practical electrocatalytic applications, we should consider factors such as the comprehensive stability and the number of active sites of the catalyst. Based on the comprehensive analysis of all data in Fig. 6, the Ru-NiCoP-O_v catalyst demonstrates excellent HER and OER catalytic activities in alkaline media, which is mainly attributed to the synergistic effect of introducing Ru atoms and oxygen defects that optimize the material's electronic structure, enhance the adsorption energy of reaction intermediates, and its unique nanosheet structure provides abundant active sites and favorable mass transfer conditions, making it a highly promising and efficient catalyst with great application prospects. As a substrate, nickel foam provides abundant active sites for the uniform loading of Ru-NiCoP-O_v active components to a considerable extent, thanks to its three-dimensional porous structure and 3D skeletal framework. This structure not only ensures excellent structural stability but also strengthens the adhesion between the catalyst and the substrate. Such characteristics prevent the catalyst from detaching or deactivating during long-term reactions. Thus, the use of

Table 2 Comparison of Ru-NiCoP-O_v electrocatalytic performance with previous literature reports

double-layer capacitance $(C_{\rm dl})$ measured by cyclic

Materials	Performances	Electrolyte	$\eta \text{ (mV)}$	Ref.
Ru-NiCoP-O _v	HER	1 M KOH	51.5 mV (-10 mA cm ⁻²)	This work
	OER		231.1 mV (10 mA cm ⁻²)	
NiCoP	OER	1 M KOH	263 mV (-10 mA cm ⁻²)	36
NiCoP	HER	1 M KOH	112 mV (10 mA cm ⁻²)	37
NiCoP	HER	1 M KOH	71 mV (-10 mA cm ⁻²)	38
	OER		268 mV (10 mA cm ⁻²)	
NiCoP	HER	1 M KOH	98 mV (-10 mA cm ⁻²)	39
NiCoP/NiFeP	OER	1 M KOH	261 mV (50 mA cm ⁻²)	40
NiCoP	HER	1 M KOH	64 mV (-10 mA cm ⁻²)	41
	OER		242 mV (10 mA cm ⁻²)	



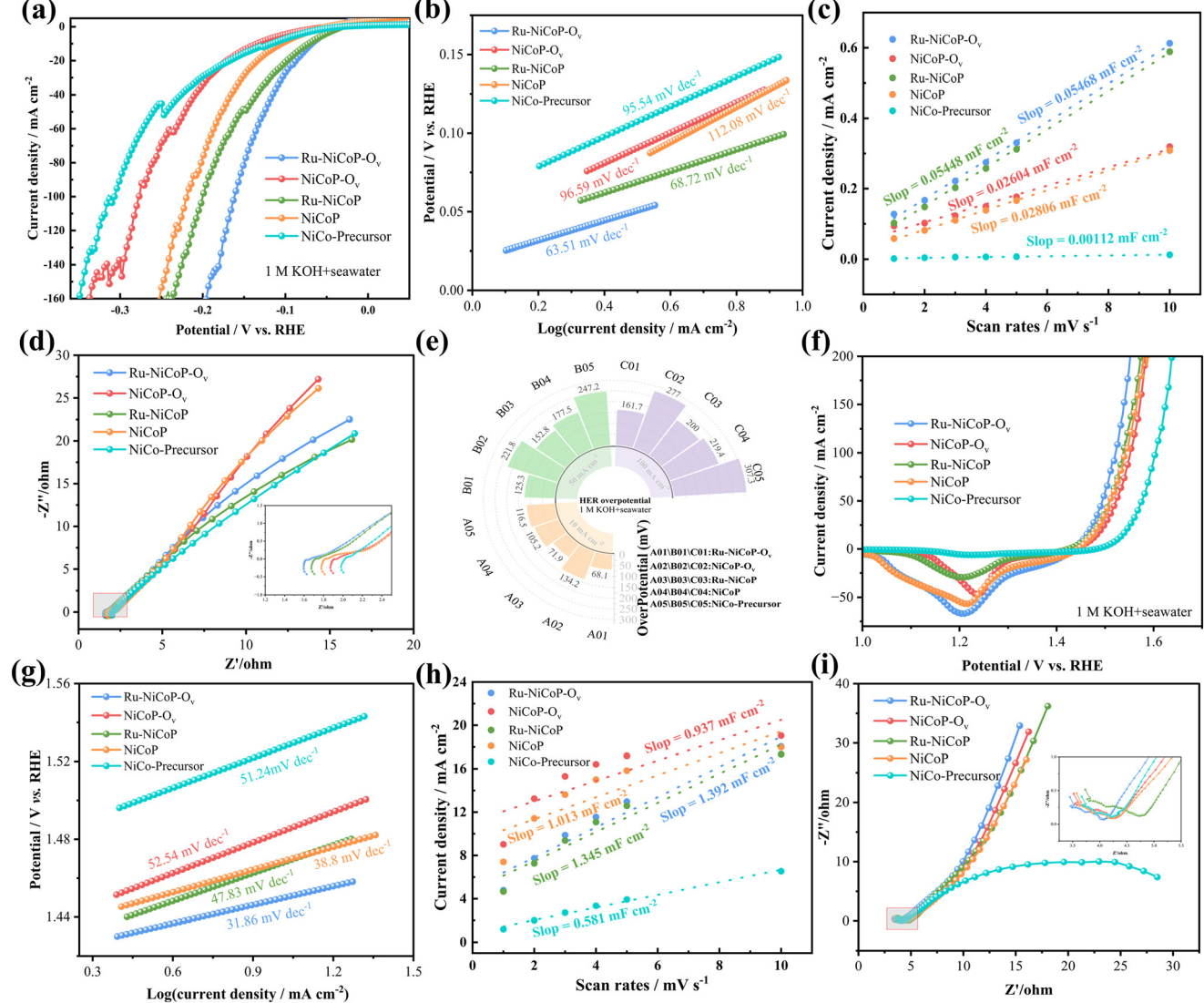


Fig. 7 HER and OER (a-i) performances in alkaline seawater (a) LSV curves of HER (b) Tafel plots (c) double-layer capacitance (d) Nyquist plots (e) radial diagram of overpotential of the sample (f) LSV curves of OER (g) Tafel plots. (h) Double-layer capacitance (i) Nyquist plots.

nickel foam as a substrate plays a crucial role in maintaining the efficiency and longevity of the catalytic system. Table 2 compares the electrocatalytic performance Ru-NiCoP-O_v with previously reported highlighting the excellent electrocatalytic performance of the sample.

Currently, research on hydrogen production through water electrolysis mostly focuses on using high-purity freshwater as the raw material. However, freshwater resources account for only 3.5% of the total global water resources, and as these resources become increasingly scarce, finding alternative water sources is becoming particularly important. The ocean nearly provides an inexhaustible source of water, with its potential hydrogen energy sufficient to meet the energy needs of future human society. 42 Therefore, hydrogen production through seawater electrolysis is considered a very promising method. In our study, we tested the electrocatalytic activity and stability of the samples in a simulated seawater environment (under 1 M alkaline conditions), providing new approaches to address future energy demands.

Subsequently, we evaluated the HER and performance of the sample electrocatalysts in a 1.0 M KOH seawater alkaline electrolyte test. Fig. 7 comprehensively showcases the hydrogen evolution reaction (HER) performance of a series of catalysts in a seawater alkaline environment (1 M KOH seawater solution). As shown in the linear sweep voltammetry curves in Fig. 7a, the curve for the Ru-NiCoP-O_v catalyst is located on the far right, indicating it has the highest current response, i.e., the strongest hydrogen production activity under the same potential, manifested as an overpotential of 68.1 mV at -10 mA cm⁻². The Tafel slope analysis presented in Fig. 7b reveals mechanistic information about the reaction; the Tafel slope for Ru-NiCoP-O_v is only

Paper CrystEngComm

63.51 mV dec⁻¹, significantly lower than that of other samples, indicating a more efficient HER reaction pathway, likely following the Volmer-Heyrovsky mechanism with the electrochemical desorption step as the rate-determining step. 43 The double-layer capacitance ($C_{\rm dl}$) test results in Fig. 7c show that by performing cyclic voltammetry at different scan rates (1-10 mV s⁻¹) and fitting the slope, the $C_{\rm dl}$ value for the Ru-NiCoP-O_v sample reaches 0.05468 mF cm⁻², markedly higher than other catalysts, indicating a larger electrochemical active surface area and richer exposed active sites. The EIS spectrum in Fig. 7d shows that in the high-frequency region, the Ru-NiCoP-O_v sample has a low semicircle diameter, implying a smaller impedance value during charge transfer. Fig. S3c† presents the impedance fitting, where Ru-NiCoP-O_v exhibits the lowest $R_{\rm ct}$ (33.23 Ω) compared to NiCoP-O_v (56.7 Ω), Ru-NiCoP (34.75Ω) , NiCoP (53.59Ω) , and NiCo-Precursor (39.55Ω) . This suggests that oxygen vacancies act as additional electron defects, promoting electron transport and providing new active sites or optimizing the electronic environment of existing active sites, thereby lowering the energy barrier for charge transfer. Consequently, the excellent charge transfer kinetics of Ru-NiCoP-O_v is one of the key factors contributing to its superior electrocatalytic performance. The radar chart in Fig. 7e further quantifies the overpotential data at different current densities, where the overpotentials for Ru-NiCoP-O_v at 10, 50, and 100 mA cm⁻² are only 68.1, 125.3, and 161.7 mV, respectively, significantly lower than those of other comparative samples. Then, we tested the oxygen evolution reaction (OER) performance of the catalysts in an alkaline seawater environment (1 M KOH seawater solution). It can be clearly observed from the linear sweep voltammetry curves in Fig. 7f that the polarization curve for the Ru-NiCoP-O_v catalyst is located on the far left, At a current density of 50 mA cm⁻², the overpotential of the Ru-NiCoP-O_v sample is 264.5 mV, which is lower than that of NiCoP-O_v (292.5 mV), Ru-NiCoP (279.5 mV), NiCoP (280.5 mV), and NiCo precursor (346.5 mV), indicating that Ru-NiCoP-O_v exhibits the highest catalytic activity for the oxygen evolution reaction. Further insights into the reaction mechanism are provided by the Tafel slope analysis in Fig. 7g; the Tafel slope for Ru-NiCoP-O_v is 31.86 mV dec⁻¹, significantly lower than NiCoP-O_v (52.54 mV dec⁻¹), Ru-NiCoP (47.83 mV dec⁻¹), NiCoP (38.8 mV dec⁻¹), and NiCo-Precursor (51.24 mV dec⁻¹), suggesting a more efficient OER reaction pathway, closely related to the optimized electronic structure due to Ru element regulation and active centers provided by oxygen defects. The double-layer capacitance (C_{dl}) test results in Fig. 7h show that through cyclic voltammetry at different scan rates (1-10 mV $\rm s^{-1}$) and fitting the slope, the $C_{\rm dl}$ value for the Ru-NiCoP-O_v sample is as high as 1.392 mF cm⁻², significantly higher than NiCoP-O_v (0.937 mF cm⁻²), Ru-NiCoP (1.345 mF cm⁻²), NiCoP (1.013 mF cm⁻²), and NiCo-Precursor (0.581 mF cm⁻²), indicating that Ru-NiCoP-O_v possesses a larger electrochemical active surface area and richer exposed active sites. In impedance plot 6i, the Ru NiCoP O_v sample has the highest semicircle diameter range in the high-frequency region

NiCoP-O_v (10.64 Ω) and Ru-NiCoP (12.04 Ω) catalysts exhibit higher Rct values compared to NiCoP-O_v (10.24 Ω), NiCoP (10.17 Ω), and NiCo-Precursor (9.53 Ω). This observation stems from their exceptionally high density of active sites. When a significant number of these active sites are rapidly occupied efficiently convert intermediates during electrochemical process, their dynamic surface adsorptiondesorption behavior profoundly influences the EIS plot. The high active site coverage induces these interfacial dynamic processes, which do not reflect an inherent reduction in the charge transfer rate. Instead, it signifies the highly efficient participation of a large number of active sites in the reaction. Comprehensive analysis of these electrochemical parameters shows that the Ru-NiCoP-Ov catalyst exhibits excellent HER and OER performance in seawater environments, mainly attributed to the synergistic effect of Ru doping and oxygen defects, which not only optimizes the electronic structure and adsorption energy but also provides more active sites and facilitates charge transfer, making it exhibit significant advantages in seawater electrolysis catalysis.

To further explore the potential application value of the prepared electrocatalysts in overall water splitting, we conducted performance tests for overall water splitting using a two-electrode setup to investigate their capability of generating hydrogen and oxygen in water splitting reactions. Fig. 8a is a schematic diagram of the setup. Fig. 8b shows the linear sweep voltammetry (LSV) curves of the series of catalysts for overall water splitting. It can be clearly observed that the curve for the Ru-NiCoP-O_v catalyst is always on the far left, indicating that it requires the lowest voltage to be applied under the same current density. Notably, as the current density increases, the performance gap between Ru-NiCoP-Ov and other materials further widens, fully confirming the significant enhancement effect of Ru modification and oxygen defects on overall water splitting performance. Particularly noteworthy is that at a high current density of 400 mA cm⁻², the voltage of Ru-NiCoP-O_v is only 1.995 V, demonstrating excellent catalytic activity for overall water splitting. Fig. 8c presents the distributed relaxation time (DRT) analysis results of the Ru-NiCoP-Ov catalyst at different voltages. This advanced electrochemical characterization technique can deeply reveal kinetic features during the catalytic process.44 The DRT spectrum shows two distinct peaks within the typical overall water splitting potential range (1.7401-1.9061 V), located in the mid-frequency region (log $\tau \approx -2$ to -1, τ approximately between 0.01 to 0.1 s) and low-frequency region (log $\tau \approx 0$ to 1, τ approximately between 1 to 10 s). As the overall water splitting voltage increases from 1.7401 V to 1.9061 V, both peaks shift significantly to smaller τ values (i.e., towards higher frequencies) and the intensity of the peaks decreases markedly, clearly indicating that the response speed of the catalytic reaction and interfacial processes significantly accelerates with the increase in voltage, leading to a significant reduction in overall impedance.

The first peak in the mid-frequency region (0.01-0.1 s) is typically closely related to fast charge transfer at the electrode interface or the adsorption-desorption process of key

compared to other samples, As illustrated in Fig. S3d,† Ru-

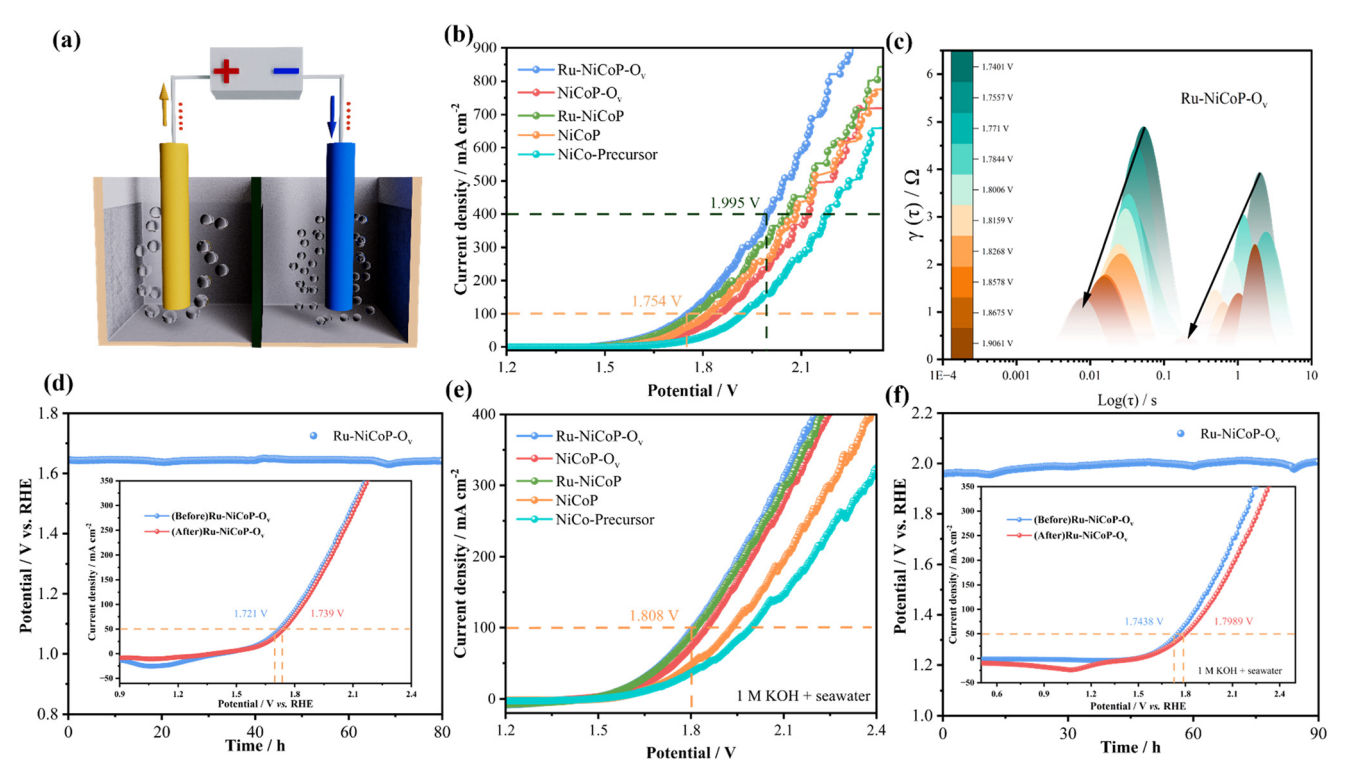


Fig. 8 Overall water splitting performance of the electrocatalysts. (a) Device schematic diagram (b) LSV curves in 1.0 M KOH (c) DRT diagram (d) overall water splitting stability for Ru-NiCoP-O_v, where the inset is LSV curves in 1.0 M KOH (e) LSV curves in alkaline seawater (f) chronoamperometric stability tests in alkaline seawater, where the inset is LSV curves.

intermediates. 45 This peak exhibits relatively high impedance (approximately 5 Ω) at a lower potential (such as 1.7401 V). As the potential increases to 1.9061 V, the impedance significantly decreases to below approximately 1 Ω . This indicates that with the increase in driving potential, the surface charge transfer or the desorption process of reaction intermediates on the electrocatalyst becomes more efficient. This phenomenon directly confirms the effectiveness of the synergistic strategy of Ru doping and oxygen defects proposed in this study: Ru doping provides an optimized electronic structure, while oxygen defects offer efficient pathways for charge and ion transport, thereby working together to reduce interfacial charge transfer impedance and promote the catalytic reaction rate.

The second peak located in the low-frequency region (1-10 s) typically corresponds to processes such as bubble formation, desorption, and mass transport diffusion of the electrolyte.46 This peak shows a significant impedance contribution (close to 4 Ω) at a lower potential (such as 1.7401 V). When the potential is increased to 1.9061 V, the impedance significantly decreases to below approximately 1 Ω , with a noticeable reduction in the characteristic time constant. This directly indicates that as the voltage increases, the rate of bubble desorption from the surface of the Ru-NiCoP-O_v catalyst and the diffusion rate of the electrolyte are significantly accelerated. Combined with SEM and TEM structural characterization of this catalyst, it is precisely because it possesses suitable hydrophilic-hydrophobic surface properties and a porous structure that it facilitates

rapid bubble detachment from the catalytic surface, thereby substantially alleviating mass transfer hindrance at the electrode interface and achieving efficient gas evolution kinetics.

To evaluate the long-term stability of the catalyst, Fig. 8d shows the constant voltage stability test results of the Ru-NiCoP-O_v catalyst. During a continuous 80 hour testing period, the Ru-NiCoP-O_v catalyst exhibited excellent stability with only minor fluctuations, confirming its structural stability and sustained activity under long-term operational conditions. The inset compares the LSV curves before and after the stability test. The results show that at a current density of 50 mA cm⁻², the voltage slightly increased to 1.739 V (compared to 1.721 V before the test). The voltage difference is only 18 mV. This minor performance decay further confirms the superior stability of the Ru-NiCoP-Ov catalyst. Fig. 8e is the LSV curve diagram under alkaline seawater conditions, clearly showing that the polarization curve of the Ru-NiCoP-Ov catalyst is located on the far left among all samples, meaning it requires the lowest voltage at the same current density. Particularly, at the key industrial application indicator of 100 mA cm⁻² current density, Ru-NiCoP-O_v requires only 1.808 V, significantly lower than other comparative samples, indicating its highest overall water splitting efficiency. Fig. 8f shows the stability test results of the Ru-NiCoP-O_v catalyst, indicating good cycling stability of the catalyst under seawater conditions. The LSV comparison curve in the inset shows that at a current density of 50 mA

cm⁻², the voltage increased to 1.7989 V after the test (compared to 1.7438 V before the test).

4. Conclusion

In summary, we have successfully synthesized a Ru-modified, oxygen-deficient NiCoP catalyst using a hydrothermal method followed by low-temperature phosphidation. The effects of Ru modification and oxygen vacancies on the material's structure and electrocatalytic performance were systematically investigated. XRD analysis confirmed that all samples successfully synthesized hexagonal phase NiCoP crystal structures, where the introduction of Ru and the creation of oxygen defects did not alter the basic crystalline phase of the materials. Electrochemical performance tests in conventional alkaline electrolyte (1 M KOH) demonstrated that the Ru-NiCoP-O_v catalyst exhibited excellent bifunctional catalytic performance, with overpotentials for HER and OER at 10 mA cm⁻² current density being 51.5 mV and 231.1 mV, respectively, significantly outperforming other control samples. In overall water splitting tests, Ru-NiCoP-Ov achieved efficient water splitting at only 1.754 V at 100 mA cm⁻² current density. In 1 M KOH seawater solution, the Ru-NiCoP-Ov catalyst also showed outstanding performance, with HER overpotential of 68.1 mV at 10 mA cm⁻² current density and OER overpotential of 264.5 mV at 50 mA cm⁻² current density (the reproducibility and structural stability of the material preparation process can be observed in Fig. S4 and summarized in Table S3†). Further overall water splitting performance tests confirmed that at 100 mA cm⁻² current density, Ru-NiCoP-Ov required only 1.808 V to achieve efficient seawater splitting, significantly lower than other comparative samples.

This study demonstrates that the synergistic strategy of "defect engineering + noble metal modification" can effectively enhance the electrocatalytic activity of NiCoP catalysts, providing new design concepts and experimental evidence for developing highly efficient and stable seawater electrolysis catalysts. It holds significant importance for promoting the development of green hydrogen production technologies driven by renewable energy.

Data availability

The data that supports the findings of this study is available from the corresponding authors upon reasonable request.

Conflicts of interest

The authors declare no conflict of interest.

Acknowledgements

This work was supported by the Project of Education Department of Liaoning Province (No. LJKMZ20220959), Science and Technology Innovation Talent Project of Liaoning Provincial Department of Education (LJ222411632049, LJ222411632081). The National Natural Science Foundation of China (No. 51971106).

References

- 1 C. Chen, J. Zhou, J. Shen, T. An, Z. Wei, Y. Zhang, S. Ju, Y. Peng, R. Fan and M. Shen, Hierarchical NiCoP/NiCo architecture on Ni mesh boosts hydrogen production under industrial alkaline conditions, *Chem. Eng. J.*, 2024, 484, 149456.
- 2 X. Zhang, J. Wang, Y. Bi, Y. Wang, Q. Liu, Y. Zhang and L. Chen, Innovative catalyst design of sea-urchin-like NiCoP nanoneedle arrays supported on N-doped carbon nanospheres for enhanced HER performance, *Langmuir*, 2024, 40, 5518–5526.
- 3 N. T. Suen, S. F. Hung, Q. Quan, N. Zhang, Y. J. Xu and H. M. Chen, Electrocatalysis for the oxygen evolution reaction: recent development and future perspectives, *Chem. Soc. Rev.*, 2017, 46, 337–365.
- 4 R. Y. Li, S. L. Xu, Z. Q. Ai, J. G. Qi, F. F. Wu, R. D. Zhao and D. P. Zhao, Interface engineering accelerated surface reconstruction for electrocatalytic water splitting and energy storage device through hybrid structured ZnCo₂O₄@NiCo-LDH nanocomposite, *Int. J. Hydrogen Energy*, 2024, 91, 867–876.
- 5 H. Zhou, R. Y. Li, S.-L. Xu, B. Zhang, R. D. Zhao, X. Zhao, F. F. Wu and D. Zhao, Interface engineering induced homogeneous isomeric bimetallic of CoSe/NiSe₂ electrocatalysts for high performance water/seawater splitting, *Adv. Sustainable Syst.*, 2024, 8, 2400849.
- 6 P. Gao, C. Yue, J. Zhang, J. Bao, H. Wang, Q. Chen and J. Zhang, Construction of unique NiCoP/FeNiCoP hollow heterostructured ellipsoids with modulated electronic structure for enhanced overall water splitting, *J. Colloid Interface Sci.*, 2024, 666, 403–415.
- 7 L. He, Z. Cai, D. Zheng, L. Ouyang, X. He, J. Chen and B. Tang, Three-dimensional porous NiCoP foam enabled high-performance overall seawater splitting at high current density, *J. Mater. Chem. A*, 2024, 12, 2680–2684.
- 8 S. L. Xu, R. D. Zhao, R.-Y. Li, J. Li, J. Xiang, F.-Y. Guo, J. Qi, L. Liu and F.-F. Wu, Constructing high-performance supercapacitors and electrochemical water splitting electrode materials through core-shell structured Co₉-S₈@Ni(OH)₂ nanosheets, *J. Mater. Chem. A*, 2024, **12**, 1595.
- 9 B. Zhang, S. L. Xu, J. Li, X. Li, R. Zhao, F. F. Wu and D. Zhao, Excellent electrocatalytic performance of CuCo₂S₄ nanowires for high-efficiency overall water splitting in alkaline and seawater media, CrystEngComm, 2025, 27, 3700–3711.
- 10 X. Zhang, Z. Wu and D. Wang, Oxygen-incorporated defectrich MoP for highly efficient hydrogen production in both acidic and alkaline media, *Electrochim. Acta*, 2018, 281, 540-548.
- 11 W. Ou, L. Li, W. Zhou, M. Chen, C. Zhu, X. Zhu and K. Yuan, Develo** a cobalt phosphide catalyst with combined cobalt defects and phosphorus vacancies to boost oxygen evolution reaction, *Materials*, 2024, 17, 4647.
- 12 A. Grimaud, A. Demortière, M. Saubanère, W. Dachraoui, M. Duchamp, M. L. Doublet and J. M. Tarascon, Activation of surface oxygen sites on an iridium-based model catalyst for the oxygen evolution reaction, *Nat. Energy*, 2016, 2, 1–10.

- 13 Q. Qian, Y. Li, Y. Liu, L. Yu and G. Zhang, Ambient fast synthesis and active sites deciphering of hierarchical foam-like trimetal-organic framework nanostructures as a platform for highly efficient oxygen evolution electrocatalysis, Adv. Mater., 2019, 31, 1901139.
- 14 H. Jang, N. Jarulertwathana, M. G. Kim and S. J. Hwang, Atomically thin holey two-dimensional Ru₂P nanosheets for enhanced hydrogen evolution electrocatalysis, ACS Nano, 2022, 16, 16452-16461.
- 15 X. Liu, W. Zhang, X. Wu and Y.-R. Cho, Porous Fe-doped Ni₃P/ CoP3 isomerism as high durable electrocatalyst for generation of hydrogen and oxygen, Energy Mater. Adv., 2025, 6, 0160.
- 16 J. Hu, X. Wang, Y. Zhou, M. Liu, C. Wang, M. Li, H. Liu, H. Li, Y. Tang and G. Fu, Asymmetric Rh-O-Co bridge sites enable superior bifunctional catalysis for hydrazine-assisted hydrogen production, Chem. Sci., 2025, 16, 1837.
- 17 X. Wang, J. Hu, T. Lu, H. Wang, D. Sun, Y. Tang, H. Li and G. Fu, Importing atomic rare-earth sites to activate lattice oxygen of spinel oxides for electrocatalytic oxygen evolution, Angew. Chem., Int. Ed., 2025, 64, e202415306.
- 18 C. Wang, X. Wu, H. Sun, Z. Xu, C. Xu, X. Wang, M. Li, Y. Wang, Y. Tang, J. Jiang, K. Sun and G. Fu, An asymmetric RE-O-Ru unit with bridged oxygen vacancies accelerates deprotonation during acidic water oxidation, Energy Environ. Sci., 2025, 18, 4276-4287.
- 19 Z. Li, Y. Yang, S. Wang, L. Gu and S. Shao, High-density ruthenium single atoms anchored on oxygen-vacancy-rich g-C₃N₄-C-TiO₂ heterostructural nanosphere for efficient electrocatalytic hydrogen evolution reaction, ACS Appl. Mater. Interfaces, 2021, 13, 46608-46619.
- 20 Q. Peng, Q. He, Y. Hu, T. T. Isimjan, R. Hou and X. Yang, Interface engineering of porous Fe₂P-WO_{2.92} catalyst with oxygen vacancies for highly active and stable large-current oxygen evolution and overall water splitting, J. Energy Chem., 2022, 65, 574-582.
- 21 Y. Wang, X. Wang, G. Chen, M. Jiang, Y. Yang, X. Gong and D. Wu, CoP-NiCoP heterojunction for enhanced bifunctional electrocatalysis in hydrogen evolution and methanol oxidation, Fuel, 2025, 384, 134042.
- 22 D. Wang, X. Huai, A. Abdukader, A. Umar and X. Wu, Highly active and durable NiCoP electrocatalyst through Ga ion intercalation strategy for long-lasting water electrolysis, Appl. Surf. Sci., 2024, 660, 159972.
- 23 Y. Lin, X. Cui, Y. Zhao, Z. Liu, G. Zhang and Y. Pan, Heterojunction interface editing in Co/NiCoP nanospheres by oxygen atoms decoration for synergistic accelerating hydrogen and oxygen evolution electrocatalysis, Nano Res., 2023, 16, 8765-8772.
- 24 S. Anantharaj and S. Noda, iR drop correction in electrocatalysis: everything one needs to know!, J. Mater. Chem. A, 2022, 10, 9348-9354.
- 25 S. Anantharaj, S. R. Ede, K. Karthick, S. S. Sankar, K. Sangeetha, P. E. Karthik and S. Kundu, Precision and correctness in the evaluation of electrocatalytic water splitting: revisiting activity parameters with a critical assessment, Energy Environ. Sci., 2018, 11, 744-759.

- 26 Z. Lv, M. Wang, D. Liu, K. Jian, R. Zhang and J. Dang, Synergetic effect of Ni₂P and MXene enhances catalytic activity in the hydrogen evolution reaction, Inorg. Chem., 2021, 60, 1604-1611.
- 27 L. Lukashuk, N. Yigit, R. Rameshan, E. Kolar, D. Teschner, M. Hävecker and G. Rupprechter, Operando insights into CO oxidation on cobalt oxide catalysts by NAP-XPS, FTIR, and XRD, ACS Catal., 2018, 8, 8630-8641.
- 28 H. Nakajima, The discovery and acceptance of the Kirkendall effect: the result of a short research career, IOM, 1997, 49, 15-19.
- 29 L. Ji, Y. Wei, P. Wu, M. Xu, T. Wang, S. Wang and Z. Chen, Heterointerface engineering of Ni2P-Co2P nanoframes for efficient water splitting, Chem. Mater., 2021, 33, 9165-9173.
- 30 Y. Liu, S. Xu, X. Zheng, Y. Lu, D. Li and D. Jiang, Ru-doped modulated cobalt phosphide nanoarrays as efficient electrocatalyst for hydrogen evolution reaction, J. Colloid Interface Sci., 2022, 625, 457-465.
- 31 S. Y. Lu, B. Huang, M. Sun, M. Luo, H. Yang and S. Guo, Synthetic tuning stabilizes a high-valence Ru single site for efficient electrolysis, Nat. Synth., 2024, 3, 576-585.
- 32 K. Fan, H. Zou and L. Duan, et al., Selectively etching vanadium oxide to modulate surface vacancies of unary metal-based electrocatalysts for high-performance water oxidation, Adv. Energy Mater., 2020, 10, 1903571.
- 33 X. Jiang, H. Jang, S. Liu, Z. Li, M. G. Kim, C. Li and J. Cho, The heterostructure of Ru₂P/WO₃/NPC synergistically promotes H₂O dissociation for improved hydrogen evolution, Angew. Chem., 2021, 133, 4156-4162.
- 34 C. X. Zhao, J. N. Liu, B. Q. Li, D. Ren, X. Chen, J. Yu and Q. Zhang, Multiscale construction of bifunctional electrocatalysts for long-lifespan rechargeable zinc-air batteries, Adv. Funct. Mater., 2020, 30, 2003619.
- 35 M. Wang, X. Liu and X. Wu, Realizing efficient electrochemical overall water electrolysis through hierarchical CoP@NiCo-LDH nanohybrids, Nano Energy, 2023, 114, 108681.
- 36 C. Yi, J. Li, L. B. Liu, S. Liu and J. L. Luo, Intellectually constructing amorphous NiCoP dendrites for efficient oxygen evolution reaction, Appl. Surf. Sci., 2023, 609, 155338.
- 37 V. S. Sumi, M. A. Sha, S. R. Arunima and S. M. A. Shibli, Development of a novel method of NiCoP alloy coating for electrocatalytic hydrogen evolution reaction in alkaline media, Electrochim. Acta, 2019, 303, 67-77.
- J. G. Wang, W. Hua, M. Li, H. Liu, M. Shao and B. Wei, Structurally engineered hyperbranched NiCoP arrays with superior electrocatalytic activities toward highly efficient overall water splitting, ACS Appl. Mater. Interfaces, 2018, 10, 41237-41245.
- 39 L. Chen, Y. Song, Y. Liu, L. Xu, J. Qin, Y. Lei and Y. Tang, NiCoP nanoleaves array for electrocatalytic alkaline H2 evolution and overall water splitting, J. Energy Chem., 2020, 50, 395-401.
- 40 J. C. Gan, L. Zhang, J. J. Feng, Y. C. Shi, X. S. Li and A. J. Wang, Self-supporting highly branched urchin-like NiCoP/NiFeP heterostructures as efficient bifunctional electrocatalyst for overall water splitting, J. Colloid Interface Sci., 2025, 687, 24-35.

- 41 C. Du, L. Yang, F. Yang, G. Cheng and W. Luo, Nest-like NiCoP for highly efficient overall water splitting, *ACS Catal.*, 2017, 7, 4131–4137.
- 42 L. Wu, L. Yu, F. Zhang, B. McElhenny, D. Luo, A. Karim and Z. Ren, Heterogeneous bimetallic phosphide Ni₂P–Fe₂P as an efficient bifunctional catalyst for water/seawater splitting, *Adv. Funct. Mater.*, 2021, 31, 2006484.
- 43 L. Zhang, H. Jang, H. Liu, M. G. Kim, D. Yang, S. Liu and J. Cho, Sodium-decorated amorphous/crystalline RuO₂ with rich oxygen vacancies: a robust pH-universal oxygen evolution electrocatalyst, *Angew. Chem.*, 2021, 133, 18969–18977.
- 44 J. Wang, Q. A. Huang, W. H. Li, J. Wang, Q. C. Zhuang and J. J. Zhang, Fundamentals of distribution of relaxation times for electrochemical impedance spectroscopy, *J. Electrochem.*, 2020, **26**, 16.
- 45 W. Shi, C. Jia, Y. Zhang, Z. Lü and M. Han, Differentiation and decomposition of solid oxide fuel cell electrochemical impedance spectra, *Acta Phys.-Chim. Sin.*, 2019, 35, 509–516.
- 46 Y. W. Lin, Y. S. Li, C. W. Chang, L. C. Huang, T. H. Yin, Y. T. Liu and Y. Choi, Kinetic analysis of oxygen evolution on spin-coated thin-film electrodes via electrochemical impedance spectroscopy, *Coatings*, 2023, 13, 1957.